

## 1 A Search for Wide-orbit Planets Around M-dwarfs using Deep MIRI 15- $\mu$ m Images

2 YIHAN LI ,<sup>1</sup> YIFAN ZHOU ,<sup>2</sup> RACHEL BOWENS-RUBIN ,<sup>3,4</sup> MARY ANNE LIMBACH ,<sup>3</sup> HANNAH DIAMOND-LOWE ,<sup>5</sup>  
3 KEVIN B. STEVENSON ,<sup>6</sup> ANDREW VANDERBURG ,<sup>7</sup> GIOVANNI STRAMPELLI ,<sup>5</sup> AND GREGORY J. HERCZEG ,<sup>8,1</sup>

4 <sup>1</sup>*Department of Astronomy, Peking University, Beijing 100871, People's Republic of China*

5 <sup>2</sup>*Department of Astronomy, University of Virginia, 530 McCormick Rd., Charlottesville, VA 22904, USA*

6 <sup>3</sup>*Department of Astronomy, University of Michigan, Ann Arbor, MI 48109, USA*

7 <sup>4</sup>*Eureka Scientific Inc., 2542 Delmar Ave., Suite 100, Oakland, CA 94602, USA*

8 <sup>5</sup>*Space Telescope Science Institute, 3700 San Martin Drive, Baltimore, MD 21218, USA*

9 <sup>6</sup>*Johns Hopkins APL, 11100 Johns Hopkins Rd., Laurel, MD 20723, USA*

10 <sup>7</sup>*Center for Astrophysics |Harvard & Smithsonian, 60 Garden Street, Cambridge, MA 02138, USA*

11 <sup>8</sup>*Kavli Institute for Astronomy and Astrophysics, Peking University, Beijing 100871, People's Republic of China*

### ABSTRACT

12 Wide-orbit (>10 AU) gas giant planets shape the architecture of planetary systems, yet their occurrence rate remains poorly constrained. JWST has obtained the deepest mid-infrared images of nearby stars to date through substantial MIRI time-series observations of transiting planets, providing sensitive probes for wide-orbit companions. Here we leverage 15 micron observations from four programs targeting ten M-dwarf systems to search for such planets. By applying reference differential imaging for precise PSF subtraction, we achieve a median  $5\sigma$  sensitivity of  $1.5 \times 10^{-3}$  (median apparent magnitude of 16.4 mag) at a separation of 1" and  $2.1 \times 10^{-4}$  (18.5 mag) at separations  $\gtrsim 3$  arcseconds. The sensitivity is converted to planet detection probability for each system as a function of planet mass versus semimajor axis. Assuming solar metallicity and clear atmosphere, we are sensitive to planets with Jupiter-like radius and 1-bar temperature ( $\sim 170$  K) at separations of 35 AU in systems at 12.5 pc. Additionally, we catalog the nearby sources and estimate their possible impact on future observations assuming they are background sources. Our results demonstrate that archival MIRI time-series imaging data is a powerful window into the population of wide-orbit gas giants around M-dwarfs.

### 25 1. INTRODUCTION

26 The James Webb Space Telescope (JWST) Mid-  
27 Infrared Instrument (MIRI) has revolutionized the char-  
28 acterization of exoplanet thermal emission. MIRI's  
29 exceptional sensitivity in the mid-infrared wavelength  
30 range has enabled detailed atmospheric studies of plan-  
31 etes across a wide range of temperatures and composi-  
32 tions (e.g., D. Powell et al. 2024; D. Valentine et al.  
33 2024). MIRI time series observations (TSO) at 15 mi-  
34 cron have been allocated over 300 hours of JWST Gen-  
35 eral Observer time for exoplanet characterization (e.g.,  
36 P. C. August et al. 2025; M. Fortune et al. 2025; N. H.  
37 Allen et al. 2025; E. A. Meier Valdés et al. 2025; M.  
38 Gillon et al. 2025). An additional 500 hours have also  
39 been allocated to the Rocky Worlds Director's Discre-  
40 tionary Time (DDT) program (S. Redfield et al. 2024).  
41 In particular, MIRI TSO have successfully captured  
42 thermal emission from temperate transiting rocky plan-

43 ets, which paves the way for identification and charac-  
44 terization of atmospheres on terrestrial exoplanets (T. P.  
45 Greene et al. 2023; S. Zieba et al. 2023).

46 JWST is a powerful planet imager. Direct imaging  
47 with JWST enables detection of cold, old, and faint ex-  
48 oplanets beyond the reach of previous facilities. The  
49 telescope has directly imaged planets as cold as 270°K  
50 (E. C. Matthews et al. 2024; W. O. Balmer et al. 2025)  
51 and discovered its first exoplanet TWA 7b with only  
52 0.3 Jupiter masses through direct imaging (A.-M. La-  
53 grange et al. 2025). MIRI imaging can detect planets  
54 with the same temperature, mass, age, and orbital sep-  
55 arations as Saturn and Jupiter (R. Bowens-Rubin et al.  
56 2025). The telescope has successfully imaged planets  
57 candidates around stars with diverse stellar types (A.  
58 Boccaletti et al. 2024; K. Franson et al. 2024), including  
59 white dwarfs (M. A. Limbach et al. 2024).

60 Time-series observations produce deep mid-infrared  
61 images as a byproduct of their primary science goals  
62 (Figure 1). These datasets capture wide fields of view  
63 and deep exposures (T. P. Greene et al. 2023; S. Zieba

et al. 2023). The exposure times are typically several hours and can be up to 59 hours in phase curve observations (M. Gillon et al. 2025). The technique of repurposing archival imaging data for serendipitous discovery has proven successful in Solar System astronomy: a recent study reported the detections of asteroids as small as 10 meters in diameter from JWST F1500W TSO data (A. Y. Burdanov et al. 2024). Similarly, differential-imaging techniques commonly used by the direct-imaging community enable searches for wide-orbit gas-giant planets in repurposed time-series observations that were originally obtained to characterize a transiting planet.

The exoplanet community has prioritized studying rocky planets around M-dwarfs, as evidenced by the 500-hour Rocky Worlds Director’s Discretionary Time program that will survey nearby M dwarf rocky planets for the presence of atmospheres. (S. Redfield et al. 2024). M-dwarf stars may be compelling targets for direct imaging searches of wide-orbit planets. Recent studies reveal a positive correlation between inner super-Earths and outer gas giants around metal-rich, Sun-like stars (M. L. Bryan & E. J. Lee 2024). This architectural relationship suggests that gas giants play a critical role in shaping planetary system formation and dynamics. (M. L. Bryan & E. J. Lee 2025) recently expanded their occurrence analysis for M-dwarf hosts. They found no correlations between inner super-Earths and outer gas giants at separations up to 10 au. However, the occurrence rate of gas giant planets around M-dwarfs beyond 10 au remains an open question. Direct imaging can address this gap. Radial velocity surveys face significant challenges around M-dwarfs due to strong stellar activity (A. Carmona et al. 2023) and the long time baselines required to detect wide-orbit companions. Additionally, the geometric probability of transit detection for planets beyond 10 AU is less than 0.03 percent. Roman microlensing observations may detect giant planets in this parameter space (e.g., M. T. Penny et al. 2019), but constraints from these observations are still years away. Direct imaging in the mid-infrared thus provides the most effective method to discover and characterize wide-orbit gas giants around nearby M-dwarfs.

In this work, we present the first performance measurement of JWST/MIRI time-series data at  $15 \mu\text{m}$  in planet direct imaging. In Section 2, we describe the archival data and reduction process. Section 3 details the method used to analyze the imaging data. Section 4 presents the performance of time-series data in both imaging sensitivity and planet detection probability. In Section 5, we compare our results with previous JWST/NIRCam and MIRI imaging performances, in-

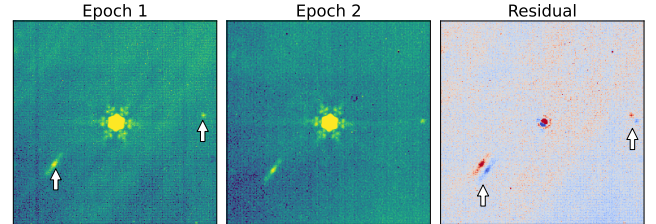


**Figure 1.** Examples of `cal.fits` images of TRAPPIST-1 observed in two epochs. The left panel shows time-series data obtained in 2020 (GTO-1177, Observation 7), and the middle panel shows a similar observation taken in 2023 (GO-3077, Observation 1). The right panel presents the residual image between these two epochs, with the target star aligned. There are two background objects on the image, denoted by arrows.

vestigate the relationship between contrast and exposure time, and discuss the implications for M-dwarf planetary system architectures. We summarize our findings in Section 6.

## 2. DATA SOURCE AND INITIAL PROCESSING

The data used in this study were obtained with JWST/MIRI in time-series observation (TSO) mode in the F1500W filter. The data set contains 33 exposures (298 segments) collected by four JWST programs: GTO-1177 (5 exposures), GO-2304 (4 exposures), GO-3077 (2 exposures), and GO-3730 (22 exposures). Table 1 lists the detailed target and observation information. The listed JWST/F1500W magnitude is calculated through aperture photometry using `photutils`.

The first three programs, GTO-1177, GO-2304, and GO-3077, targeted TRAPPIST-1, an M-dwarf hosting seven transiting terrestrial planets (M. Gillon et al. 2017; E. Ducrot et al. 2025). The last program, GO-3730, targeted nine M-dwarfs hosting transiting rocky planets (e.g., P. C. August et al. 2025). The F1500W ( $\lambda_0 = 15.0 \mu\text{m}$ ,  $\Delta\lambda = 2.92 \mu\text{m}$ ,  $\text{FWHM}=0.488''$ ) imaging time series were initially acquired to characterize the secondary eclipses of the transiting terrestrial planets. The long exposures provide sensitivity enabling the direct detection of wide-orbit giant planets.

We downloaded the `jwst` Stage 1 pipeline products (`rate` files) from the MAST archive. The `rate` files were used instead of the `rateints` files, because the point spread function (PSF) is extremely stable between integrations of the same exposure. Therefore, using individual integrations provided in `rateints` files does not enhance the diversity of reference PSF or improve PSF subtraction but substantially increases the computational cost (J. Kammerer et al. 2024). The `rate` files were then processed with the `jwst` Stage 2 pipeline (ver-

**Table 1.** Survey Targets and Observing Information

Name	Distance (pc)	Total exposure time (hours)	<i>K</i> (mag)	F1500W (mag)	Spectral Type	<i>N</i> planets
GJ 3473	$27.31 \pm 0.02$	12.86	8.829	8.35	M4.0	2
LHS 1140	$14.96 \pm 0.01$	11.02	8.821	8.20	M4.5	2
LHS 1478	$18.21 \pm 0.01$	6.10	8.767	8.26	M3.5	1
LTT 3780	$22.03 \pm 0.01$	6.00	8.204	7.74	M4.0	2
TOI-1468	$24.72 \pm 0.02$	10.84	8.05	8.17	M3.0	2
TOI-270	$22.48 \pm 0.01$	16.14	8.251	7.86	M3.0	3
TRAPPIST-1	$12.47 \pm 0.01$	86.35	10.296	9.48	M7.5e	7
HD 260655	$9.998 \pm 0.002$	6.73	5.862	5.54	M0.0	2
L 98-59	$10.608 \pm 0.002$	3.34	7.101	6.71	M3.0	5
GJ 357	$9.436 \pm 0.002$	4.03	6.475	6.06	M2.5	3

NOTE—The information of our targets. Distances are calculated from Gaia Data Release 3 ( [Gaia Collaboration et al. 2016, 2023](#)). The exposure time for each target is the total measurement time of all exposures used. The K-band magnitude and spectral type are obtained from SIMBAD. The “N planets” column represents the number of known planets based on NASA Exoplanet Archive.

sion 1.17.1). In this step, WCS is assigned, the flat field is calibrated, and the flux units are converted to MJy/sr. We unified the data dimensions by cropping all images (except for three targets listed below) to  $252 \times 252$  pixel<sup>2</sup> centered on the target (field of view:  $27.8'' \times 27.8''$ , pixel size:  $0.11''$ ). Three targets are observed with even smaller subarrays: L 98-59 uses SUB128, and target HD 260655 and GJ 357 use SUB64. Therefore, we cropped these images to  $40 \times 40$  pixel<sup>2</sup> (field of view:  $4.4'' \times 4.4''$ ).

To prevent spurious pixels from affecting PSF subtraction analysis, we identified and corrected three types of “bad pixels”. The first type is pixels flagged as “DO NOT USE” by the `jwst` pipeline. The second type is spurious background pixels missed by the pipeline. To identify them, we applied a sliding window (10 pixels  $\times$  10 pixels) and flagged isolated pixels with values exceeding the local median by  $5\sigma$ . Regions within 25 pixels of the central star were excluded because the large flux gradient makes median and standard deviation in a square window unreliable. The third type is bright isolated pixels lying within 25 pixels of the stellar centroid. These anomalous pixels appeared in small numbers, with typically one or two detected per exposure. We identified these pixels using the same  $5\sigma$  criterion but with an annulus window ( $r_{\text{in}} = 13$  pixels,  $r_{\text{out}} = 25$  pixels). We replaced all detected pixels by bilinear interpolation from neighboring pixels.

3. PSF MODELING AND SUBTRACTION

### 3.1. KLIP

PSF subtraction is performed via KLIP ([R. Soummer et al. 2012](#)), an algorithm subtracts the stellar PSF from the target images, based on Principal Component Analysis (PCA). We used reference differential imaging (RDI) to construct and subtract the host star PSFs. For each set of target images, a dedicated PSF library is assembled.

### 3.2. PSF Library

We first assemble a PSF library to perform RDI on each target star. A key challenge is that the PSF shape depends on detector position. To account for this variation, we categorize the PSF library by subarray type, using only images taken with the same subarray as mutual references. However, two exceptions apply. First, TRAPPIST-1 was observed with the FULL (GTO-1177 and GO-2304) and BRIGHTSKY (GO-3077) subarrays, neither of which is shared by any other target in our study. Consequently, we use images from the other nine targets as references for TRAPPIST-1 despite the subarray mismatch. Second, three bright sources were observed with small subarrays (SUB128 and SUB64), which collectively provide only ten reference images. To ensure a sufficiently large PSF library, we include all images targeting the other seven stars as references, regardless of subarray.

We align the target and reference images by PSF centers. The PSF centers are determined by fitting model

PSFs. To account for the detector’s geometric distortion and the resulting spatial variations in the PSF shape, we create a grid of 49 model PSFs using `stpsf` distributed across the full detector. Next, a `photutils` PSF model class, `GriddedPSFModel`, is created using the model PSF grid. All cropped images are extended to the size of the full detector according to their original subarray configurations, so that the target’s coordinates in the extended image match its actual location on the detector. We use `photutils` to interpolate four PSFs in the grid that are closest to the target position to get a model PSF. We find the best-fitting scaling and centroid coordinates using a nonlinear least-squares approach (L. Bradley et al. 2025). The images in the PSF library are then aligned to a common central coordinate.

### 3.3. KLIP Parameter Optimization

Optimizing the KLIP parameters is essential, as they significantly affect PSF subtraction performance. During KLIP modeling, images are divided into multiple annuli and position-angle (PA) sectors. KLIP is performed on these image subregions independently. The number of principal components (KL modes) controls the aggressiveness of the PSF subtraction. Increasing both the number of subregions and principal components allows for more precise modeling of the stellar PSF and more thorough suppression of starlight. However, this also increases the risk of oversubtraction and potentially removing planetary signals (L. Pueyo 2016). Here we follow the method described in J. I. Adams Redai et al. (2023) to explore the optimal KLIP parameters.

The injection and recovery of model PSFs is a key step for evaluating the PSF subtraction performance (L. Pueyo 2016). In our case, we generate synthetic planet PSFs by interpolating the model PSF grid produced by `stpsf` at the host star position (also see Section 3.2). These synthetic PSFs, with fixed total flux approximately 20 times the local noise level, are injected into the `cal.fits` images at separations of 5, 20, 60, and 100 pixels. To account for azimuthal variations, we place four PSFs at each separation, spaced 90 degrees apart in position angle. For the three targets using smaller subarrays, we inject only one PSF at each of three separations (5, 10, and 15 pixels), with the three PSFs separated by 90 degrees in position angle. The modified images are then processed with KLIP using identical parameters as the science data. After PSF subtraction, we measure the recovered flux of each injected signal within a circular aperture of diameter 4.436 pixels, corresponding to

the PSF FWHM for F1500W from the JWST documentation<sup>9</sup>.

We evaluate the performance of each KLIP parameter set using image quality metrics proposed by J. I. Adams Redai et al. (2023), including the Contrast Curve, Peak S/N, Neighbor Quality, and False Positive Fraction.

#### 3.3.1. Contrast

The Contrast metric is defined as the calibrated  $5\sigma$  noise at separations of 5, 20, 60, and 100 pixels. We first obtain the raw contrast curve by computing the  $5\sigma$  noise using a ring of apertures (diameter 4.436 pixels) at each separation between 3 and 100 pixels. The throughput correction factor is calculated as recovered PSF flux/injected PSF flux, averaged over the four PSFs at each separation. We obtain the throughput curve by linearly interpolating values at separations with injected PSFs (5, 20, 60, and 100 pixels) and extrapolating to the inner (3-5 pixels) region. The calibrated contrast curve is then obtained by dividing the raw  $5\sigma$  noise by the throughput curve. Following J. I. Adams Redai et al. (2023), we normalize the calibrated contrast values at the injection separations and take their mean value as the Contrast metric for each parameter set.

#### 3.3.2. Peak S/N

The Peak S/N is defined as the peak S/N of the recovered model PSF. The PSF-subtracted image is first masked to exclude background sources, then divided into concentric annuli centered on the star. Within each annulus, we compute the standard deviation and compiled these values to generate a radial noise map assuming azimuthal symmetry. The final S/N map is then produced by dividing the model-PSF-injected image by this noise map. We then compute the Peak S/N as the averaged peak S/N of injected PSFs.

#### 3.3.3. Neighbor Quality

The Neighbor Quality is computed by smoothing the Peak S/N metric across number of KL modes/annuli space with a Gaussian kernel. This process averages the performance of adjacent parameter sets. As a result, when evaluating a given set of KLIP parameters, both its individual performance and the robustness of its local neighborhood are considered, helping to identify more stable solutions.

#### 3.3.4. False Positive Fraction

The False Positive Fraction is defined as the number of pixels whose values are higher than the local  $5\sigma$  noise,

<sup>9</sup> <https://jwst-docs.stsci.edu/jwst-mid-infrared-instrument/miri-performance/miri-point-spread-functions>

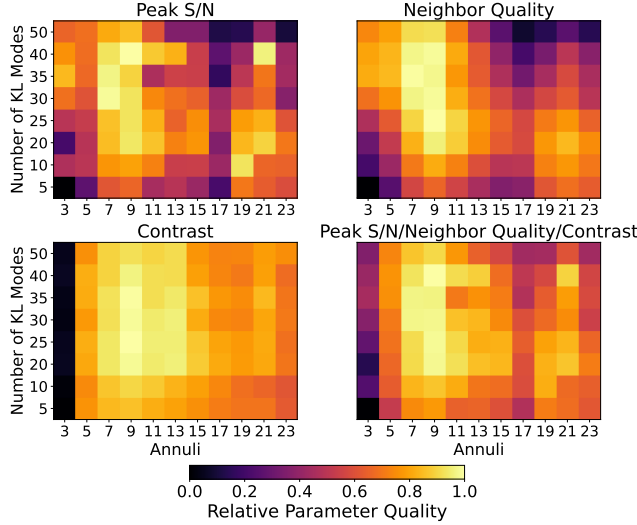


**Figure 2.** Map of image metrics across numbers of KLIP basis and annuli parameter space for TRAPPIST-1. The lower right show the quality of parameters measured by the combination of these metrics. Each pixel's color represents the relative quality of that parameter combination, with 1 being the best and 0 being the worst. The False Positive Fraction metric is nearly uniform across parameter space and has minimal effect on the combined metrics. We therefore selected optimal parameters based on the combined Peak S/N, Neighbor Quality, and Contrast metrics.

within the region between the inner and outer working angles on the PSF-subtracted image. Real background sources are excluded when counting false positive pixels.

We normalize each metric following the procedure described in (J. I. Adams Redai et al. 2023), scaling values so that the best-performing parameter set has value 1 and the worst has value 0. For Peak S/N and Neighbour Quality, the best parameter set gives the highest S/N of a recovered PSF injection. For Contrast, the best set produces the lowest  $5\sigma$  contrast at injection separations. For False Positive Fraction, the best set minimizes the number of false positive pixels. Finally, we compute the average of the four metrics: Peak S/N, Neighbor Quality, Contrast, and False Positive Fraction to evaluate the parameters. Since the False Positive Fraction is nearly uniform across the parameter space and contributes negligibly to distinguishing between parameter sets, we exclude it from the final evaluation. Instead, we take the average of the remaining three metrics as the standard for selecting the optimal parameter set.

We explore the number of KL modes and annuli parameter space and determine the optimal number of KL modes and annuli parameters for each target using the method described above. Figure 2 shows the image metric maps across parameter space for TRAPPIST-1. For the seven targets with larger fields of view, the optimal

**Table 2.** Optimal KLIP Parameters

Target	Number of KL modes	Number of Annuli
GJ 3473	25	9
LHS 1140	25	23
LHS 1478	20	21
LTT 3780	40	13
TOI-1468	25	9
TOI-270	10	19
TRAPPIST-1	40	9
HD 260655	15	4
L 98-59	5	6
GJ 357	25	4

number of KL modes falls between 10 and 40, with annuli values ranging from 9 to 23. For the other three bright sources, the optimal number of KL modes lies between 5 and 25, and the corresponding annuli range from 4 to 6. Due to the small image size of the three bright sources, we explored relatively small annuli values (1 to 8) to ensure there are enough pixels inside each annuli.

### 3.4. Image Analysis

We perform PSF subtraction on each target using the optimal KLIP parameters listed in Table 2 and obtain the PSF-subtracted images. Upon examining these images, we identify marginally significant residuals (peak S/N 2-3) within 15 pixels of the stellar center for four targets. An example of GJ 3473 is presented in Figure 3 (upper right panel).

To determine whether these residuals are artifacts or real signals, we conduct two diagnostic tests. First, we perform KLIP using ten different subsets of the reference image library to determine whether the residuals are artifacts arising from specific reference frame combinations. The residuals persist across all reference subsets with peak S/N values consistently between 2 and 3, indicating they are not caused by particular reference PSF selections.

Second, we perform KLIP on each individual exposure of a given target separately to test whether these residuals are artifacts that originate from specific exposures. As shown in Figure 3, all targets with strong central residuals contain one individual exposure that already displays similar residual features before stacking. Since the exact origin of these residuals remains unclear and requires further investigation, we conserva-

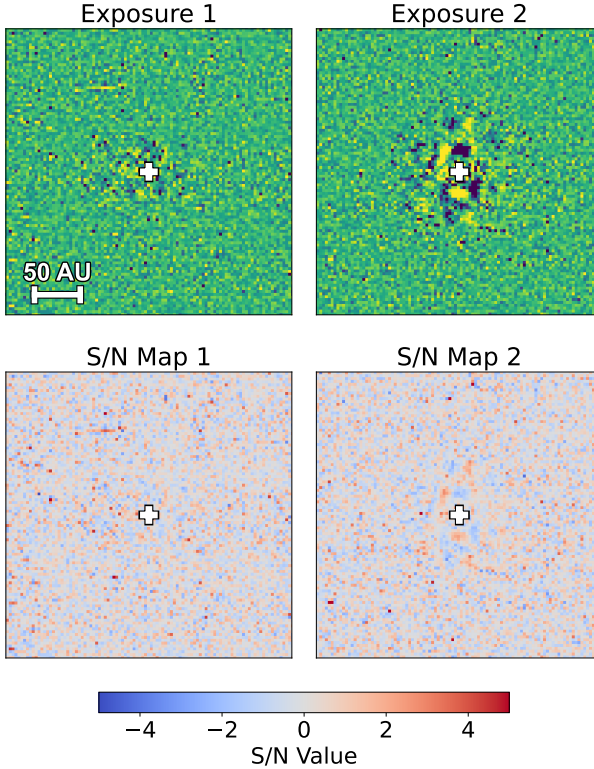


**Figure 3.** PSF-subtracted images of two exposures targeting GJ 3473 and the corresponding S/N maps. The upper left image shows a clean PSF subtraction while the upper right image presents apparent residuals near the central star. The peak S/N of these residual patterns is  $\sim 2.8$  (lower right panel). North is up and east is to the left.

tively exclude the affected exposures from our analysis and present KLIP results based only on the remaining clean exposures.

Figure 4 shows the PSF-subtracted images of all targets after removing the affected exposures.  $100 \times 100$  pixel area ( $11.0'' \times 11.0''$ ) highlights the region close to each central star for the first seven targets. Figure 5 shows the corresponding S/N maps of these images.

Figure 6 shows the  $5\sigma$  contrast curves, computed as in the same way described in Section 3.3. To convert the  $5\sigma$  noise to contrast units, we determine the brightness of our target stars by aperture photometry using `photutils`. We calculate the raw star flux using a  $r = 2.218$  pixel ( $\text{FWHM}/2$ ) radius aperture. The background level is estimated within an annulus with radius ranging from 40 to 50 pixels (15 to 20 pixels for targets with smaller field of view) and subtracted from the raw star flux. We derive the contrast curve in plant flux/star flux unit by dividing the  $5\sigma$  noise curve by the estimated star flux. Additionally, we convert the  $5\sigma$  noise sensitivity curve to apparent magnitude using

function `flux_to_magnitude` from `species` (T. Stolk et al. 2020). Figure 6 shows the  $5\sigma$  noise and apparent magnitude contrast curves for all targets.

## 4. RESULTS

### 4.1. Primary Subtraction Results

Figure 4 and Figure 5 present the PSF-subtracted images and their corresponding S/N maps. Three of our targets show point sources within  $5.5''$  of the central star. Source LHS 1478-A has  $S/N = 24.1$ . Source A, B, and C around TOI-1468 has  $S/N = 47.6, 11.2$ , and  $6.7$ . Source TOI-270-A has  $S/N = 14.1$ .

Additionally, HD 260655 shows a point-source-like signal with  $S/N$  of 4.86 (denoted by an arrow) within  $2''$ . We present the 1D profile in Section 4.3. LHS 1478 and LHS 1140 both show line-shaped detector artifacts located to the south and west, respectively.

The  $5\sigma$  sensitivity and apparent magnitude contrast curves are shown in Figure 6. We achieve a median  $5\sigma$  sensitivity of  $1.1 \times 10^{-2}$  (median apparent magnitude of 14.2 mag) at a separation of  $0.5''$  and  $2.1 \times 10^{-4}$  (18.5 mag) at separations  $\gtrsim 3''$ . The contrast curves become deeper as the separation increases within the first  $2''$ . Beyond that, the curves become background-limited and remain roughly constant.

Differences of  $5\sigma$  contrast between targets are due to different luminosity and exposure time of each source. With the same exposure time,  $5\sigma$  noises are of the same order in the background-limited region. As a result, fainter targets tend to have a worse contrast. TRAPPIST-1, the faintest star in our study, shows the worst contrast at background-limited region, despite its much longer total on-source integration time. Other than TRAPPIST-1, TOI-270 has the longest exposure time and has the deepest contrast curve. Targets HD 260655, L 98-59, and GJ 357 are much brighter, so they were observed with SUB128 and SUB64 to avoid saturation. Consequently, their contrast curves are limited to separations within  $\sim 2''$ . In addition, as described in Section 3.2, we include images using different subarrays as references. Their different positions on the detector hindered our ability to capture the detailed structure of the star PSF, leading to poorer PSF subtraction. As a result, the contrast curves for these bright sources are not as deep, as shown in Figure 6.

### 4.2. Detection Sensitivity

We use the observed contrast curves to evaluate planet detection sensitivity as a function of planet mass and semimajor axis following (E. Bogat et al. 2025). Substellar evolutionary models, `BEX-petitCODE` (E. F. Linder et al. 2019) and `ATMO-CEQ` (M. W. Phillips et al. 2020),

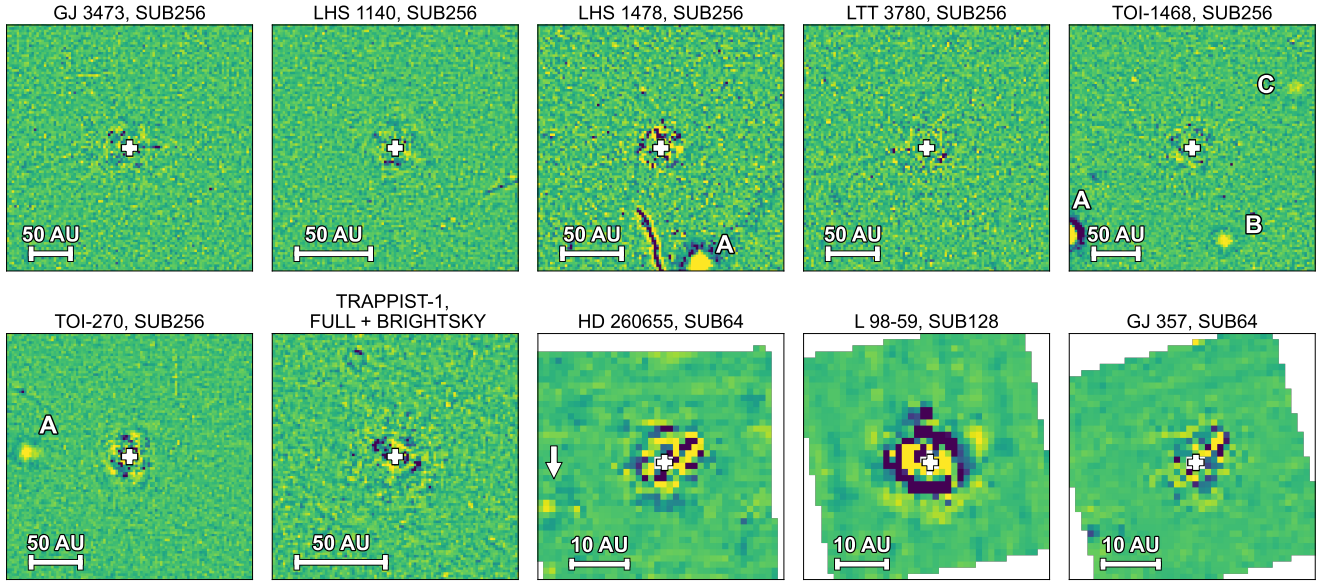


**Figure 4.** PSF-subtracted images of all targets. The observation subarray of each target is indicated. The first seven images are zoomed in to area of  $11.0'' \times 11.0''$  for clearer view of the central regions. For the last three targets, the small size ( $4.4'' \times 4.4''$ ) is due to the choice of the observation subarray. The location of the star PSF center is denoted by the white cross. Sources around LHS 1478, TOI-1468, and TOI-270 are labeled with letters. The arrow near HD 260655 indicates a low-S/N identification of possible close companion. We further examined this detection in Section 4.4. North is up and east is to the left.

are adopted to translate apparent magnitude limits into mass limits at specific ages. We use Monte Carlo calculations to convert semimajor axes into projected angular separations, allowing us to compute detection probabilities across a range of orbital configurations.

To implement this approach, we create a mass-semimajor axis grid ranging from 1 to  $20 M_{Jup}$  and 1 to 500 AU, sampled with 100 mass values and 100 semi-major axis values uniformly spaced in logarithmic scale. For each planet mass in our grid, we estimate a planet's F1500W absolute magnitude by interpolating evolutionary model grids. We then convert these absolute magnitudes to apparent magnitudes using target distances from Gaia Data Release 3. For masses below  $2 M_{Jup}$ , we use the BEX-petitCODE model. We use the solar metallicity and cloudless assumptions as our nominal case and explore the impact of different metallicity and cloud assumptions below. For masses above  $2 M_{Jup}$ , we use the ATMO-CEQ chemically equilibrium model. This combination follows the approach of E. Bogat et al. (2025).

Four of our targets have age constraints: TRAPPIST-1 ( $7.6 \pm 2.2$  Gyr; (A. J. Burgasser & E. E. Mamajek 2017)), LHS 1140 ( $> 5$  Gyr; (J. A. Dittmann et al. 2017)), HD 260655 (2-8 Gyr; (R. Luque et al. 2022)), and L 98-59 ( $4.94 \pm 0.28$  Gyr; (S. G. Engle & E. F. Guinan 2023)). Therefore, we adopt 5 Gyr as the nom-

inal age and explore alternative ages 100 Myr, 1 Gyr, and 10 Gyr. The BEX-petitCODE model does not extend below  $2 M_{Jup}$  at 5 Gyr, so we extrapolate its 1-2  $M_{Jup}$  mass range to this age linearly in log age space. Similarly, the ATMO-CEQ model is limited to  $\gtrsim 4 M_{Jup}$  at 5 Gyr and is extrapolated to lower masses using the same method.

For each semimajor axis in our grid, we calculate a projected separation via Monte Carlo sampling. Following E. Bogat et al. (2025), we assume a Gaussian distribution with mean of 0 and sigma of 0.1 for orbital eccentricities, an isotropic distribution of inclination (i.e.,  $\cos i$  is uniformly distributed,  $i$  is the inclination angle), and a uniform distribution for the argument of periaxis. To simplify the calculation, we also assume a uniform distribution of the true anomaly, which serves as a good approximation for nearly circular orbits. At each grid semimajor axis, the projected separation is calculated accordingly. A model planet is considered detectable if its apparent magnitude is brighter than the sensitivity at the projected separation. This Monte Carlo simulation is repeated 1,000 times per grid point to derive the detection probability across the parameter space.

Figure 7 shows the detection sensitivity calculated assuming a 5 Gyr age, solar metallicity, and cloud-free atmospheric model. Our sensitivity is limited by con-

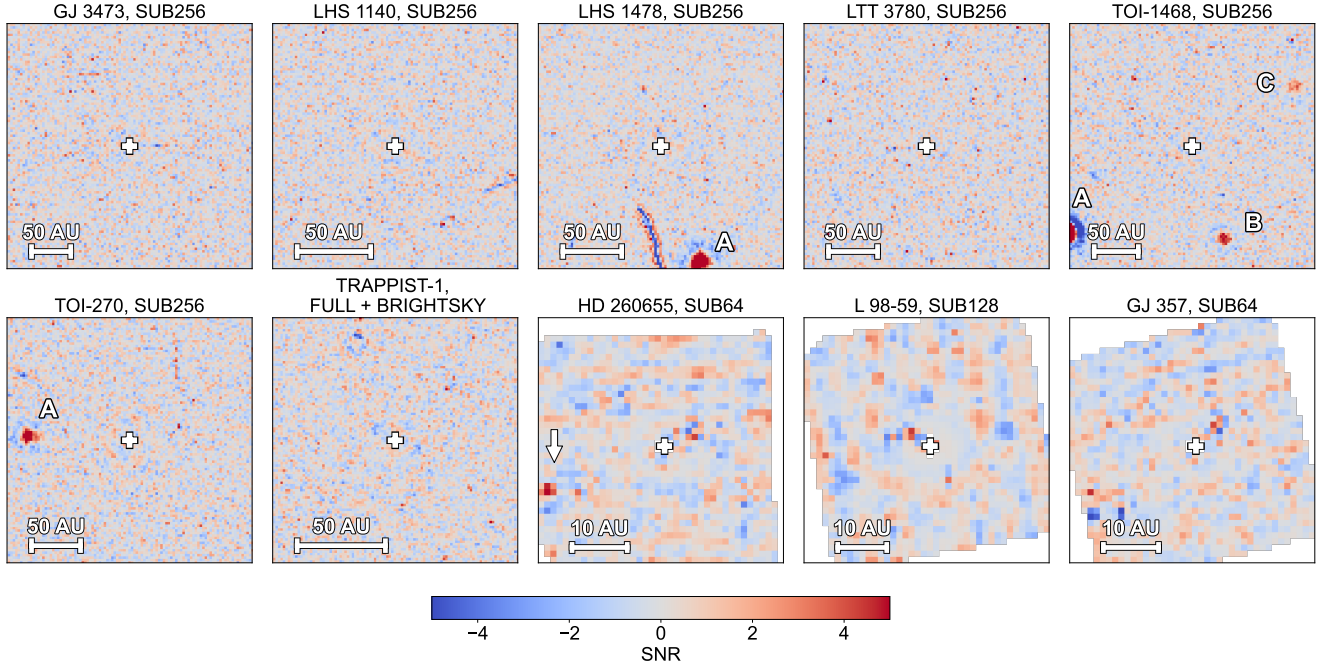


**Figure 5.** Signal-to-noise ratio maps of all targets. Figure annotations follow the same convention as Figure 4.

trast at 5 AU for LHS 1140 and 10 AU for TOI-270. As a result, no planets below  $20 M_{Jup}$  can be detected at smaller semimajor axis. The sharp cutoff of detection probability at  $2 M_{Jup}$  is a numerical artifact arising because the BEX-petitCODE model predicts much fainter brightness for low-mass planet ( $M < 2 M_{Jup}$ ) after extrapolation.

Except for the three targets observed with small subarrays, we can detect planets as small as  $4 M_{Jup}$  at 10 AU semimajor axis. The sensitivity improves with increasing semimajor axis, reaching  $\lesssim 2 M_{Jup}$  sensitivity beyond 30 AU. Assuming the same system age of 5 Gyr, the LHS 1140 and TRAPPIST-1 observations provide the best performance, with detection limits down to  $2 M_{Jup}$  at 15 AU. For solar metallicity and cloud-free atmospheres, we are sensitive to planets with Jupiter-like radius and 1-bar temperature ( $\sim 170$  K, P. Gupta et al. 2022) at separations of 35 AU in systems at 12.5 pc. For the three bright targets observed with smaller subarray, the sensitivity also drops to zero within 10 AU semimajor axis. At around 10 AU, we are sensitive to as small as  $5 M_{Jup}$ . Beyond 30 AU, the sensitivity for these three targets is cut off due to the limited image field of view.

We use TRAPPIST-1 to demonstrate how stellar age and atmospheric assumptions affect detection probability. The BEX-petitCODE model does not extend to 1 Gyr for masses below  $1 M_{Jup}$ , or to 10 Gyr for masses below  $2 M_{Jup}$ , and the ATMO-CEQ model is limited to  $\gtrsim 4$

$M_{Jup}$  at 5 Gyr and  $\gtrsim 5 M_{Jup}$  at 10 Gyr. We therefore apply the same linear extrapolation in log age space to cover lower masses at the older ages.

The detection sensitivity worsens as the assumed age increases for cloud-free, solar metallicity models (Figure 8, upper panel). At 100 Myr, we can detect a Saturn-mass ( $0.3 M_{Jup}$ ) planet at 20 AU with 50% probability. At 5 and 10 Gyr, the results are strongly influenced by model extrapolations. The cutoffs at  $2 M_{Jup}$  arise from model extrapolation as described before. Our detection map is valid for mass greater than  $5 M_{Jup}$ . Validating our results relies on extending evolutionary models with masses below  $5 M_{Jup}$  to ages older than 5 Gyr.

We then fixed the age at 5 Gyr to examine how atmospheric metallicity and cloud properties affect planet detection probability for TRAPPIST-1. Increasing atmospheric metallicity or introducing clouds enable detecting lower mass planets (Figure 8, lower panel). This improvement in sensitivity is consistent with trends in evolutionary models discussed in (E. F. Linder et al. 2019). For atmosphere with the highest metallicity of  $[M/H]=1.2$  and with clouds, we can detect planet of  $0.8 M_{Jup}$  ( $> 50\%$  detection probability).

#### 4.3. Close Companion Sources

Figure 9 shows that for stars GJ 3473, LHS 1478, TOI-1468, TOI-270, and TRAPPIST-1, we detect nearby sources within 50 arcsec. We measure their astrometry

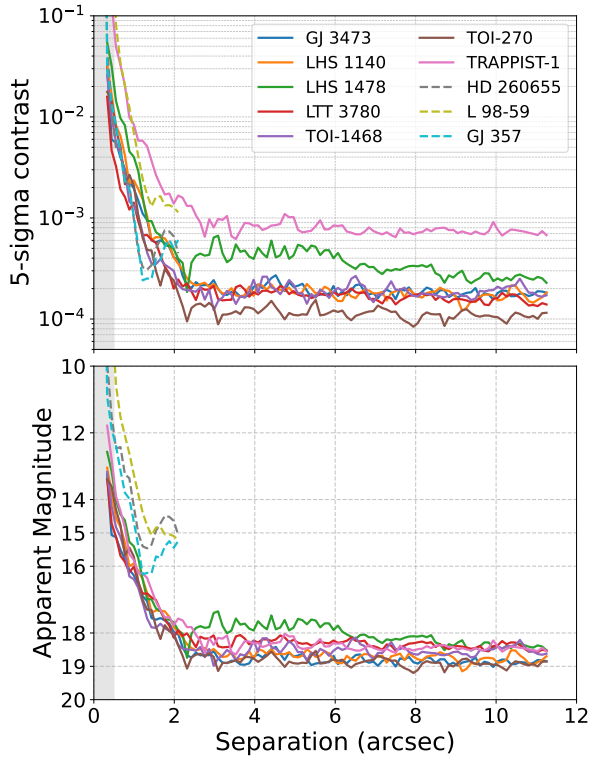


**Figure 6.** Survey sensitivity in  $5\sigma$  contrast (upper panel) and apparent magnitude (lower panel). The three bright targets HD 260655, L 98-59, and GJ 357 are observed with smaller subarrays, thus limiting the curves to  $\sim 2''$ . The shaded area within  $0.5''$  indicates the region where the throughput curve is extrapolated (see Section 3.3). The sensitivity in contrast differs from target to target, due to differences of central star brightness and exposure time.

and photometry using PSF forward modeling with the `pyKLIP.fm` module. The FWHM of each source is measured using `lmfit` to distinguish between point sources and extended objects. We estimate the potential masses of point sources assuming they are substellar companions. Furthermore, we predict the future relative positions of these sources with respect to the target stars under the assumption that they are background objects.

PSF forward modeling is a necessary step to correct for flux loss caused by PSF subtraction (L. Pueyo 2016). A model PSF is generated from interpolating the `stpsf` grid and normalized to a total flux of 1. We scale this model PSF to an initial approximate flux and inject it at the same position as the background source in a simulated blank image matching the science image size. PSF subtraction is performed to both the science image and the simulated PSF model image using the same KLIP parameters to create a forward model. This model is then fit to the background source. A Markov Chain

Monte Carlo (MCMC) algorithm is adopted to find the best-fitting flux scaling factor and coordinates. To assess source morphology, we fit the FWHM of each source using a custom rotational 2D Gaussian model with `lmfit`. Sources whose major axis FWHM exceeds  $3\sigma$  of the expected point source FWHM (4.436 pixels) are categorized as extended sources. Table 3 lists the relative positions to the star, detection S/N, brightness, and fitted FWHM along major and minor axes.

We estimate their masses assuming they are substellar companions using both the `BEX-petitCODE` model (for  $< 2M_{Jup}$ ) and the `ATMO-CEQ` model (for  $> 2M_{Jup}$ ). Their apparent magnitudes are converted to absolute magnitudes using the distance of its central star. We obtain the corresponding masses from the models at ages of 1 Gyr, 5 Gyr, and 10 Gyr. Magnitudes from the `BEX-petitCODE` grids are extrapolated to these three ages in logarithmic age space. For 1 Gyr, the lower magnitude limit of the `ATMO-CEQ` model is 14.22 mag, while the upper limit of the `BEX-petitCODE` model is 14.84 mag. Therefore, magnitudes between these two values lie outside both models. We did not extrapolate the `ATMO-CEQ` grids in age or extrapolate the `BEX-petitCODE` grids in magnitude to keep our results robust, instead we give the upper and lower mass limit predicted by the two grids. For 5 Gyr, the gap ranges from 14.67-17.94 mag. For 10 Gyr, it is 15.00-19.27 mag. The estimated mass for those that are not obvious extended sources is listed in Table 3. As shown in Figure 1, two programs targeting TRAPPIST-1 at different epochs demonstrate that the two sources near TRAPPIST-1 are not co-moving with the star. We therefore rule them out as substellar companions and classify them as background sources in the table.

We assess the possible impact of these sources on future observations, considering the differences in proper motion between the planet host stars and background sources. Sky coordinates, distances, and proper motions of each target are retrieved from the Gaia Data Release 3. Using these data, we compute the positions of each target at the observation epoch and at J2040 by propagating the Gaia coordinates with their proper motions. Figure 9 shows the estimated positions at J2040, with target stars marked by red crosses. For GJ 3473, TOI-1468, and TOI-270, the target star will approach within  $2''$  of a nearby source, which could contaminate future observations.

#### 4.4. Faint Companions Within 20 AU Separation

Figure 4 and Figure 5 reveal a point-source-like residual near the central star HD 260655 (peak S/N 4.86). To determine whether this is an astrophysical signal or ar-

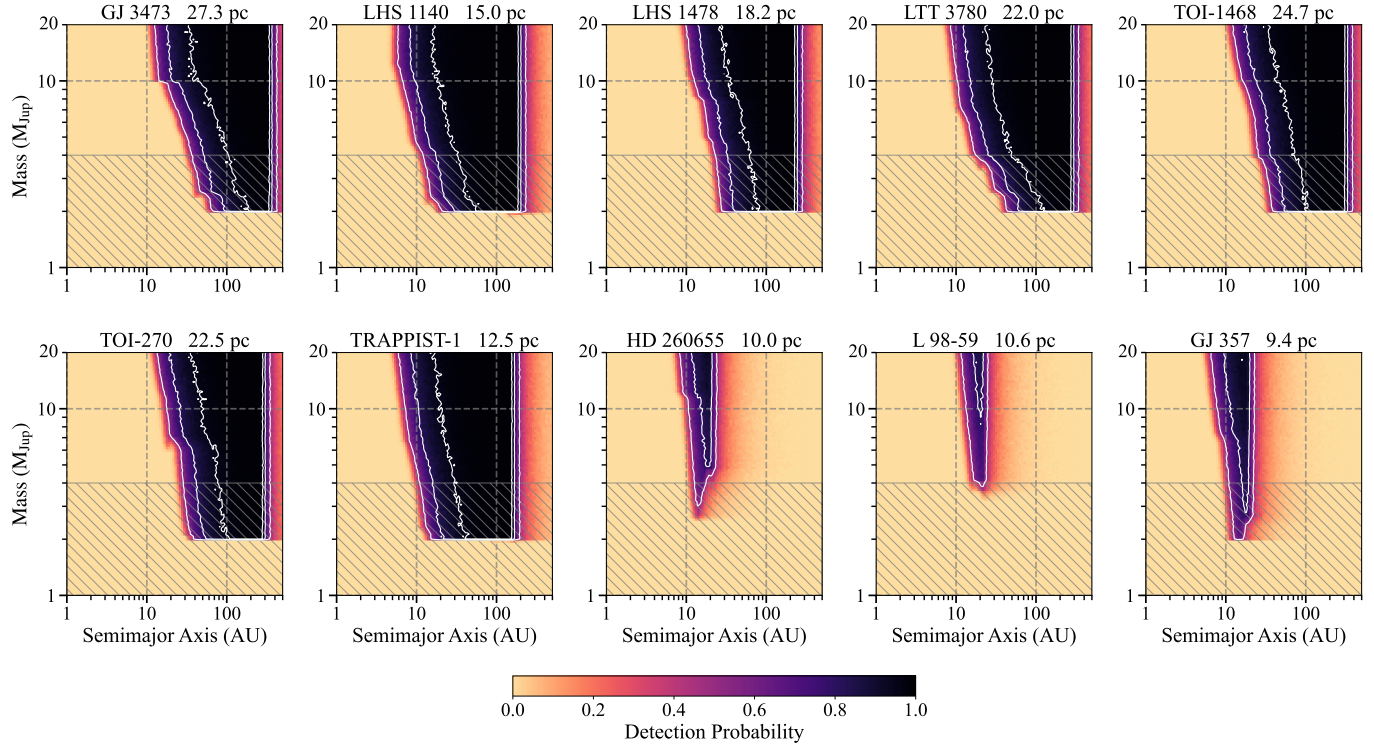


**Figure 7.** Detection probability map as a function of planet mass versus semimajor axis, assuming system age of 5 Gyr, solar metallicity and a cloud-free atmosphere model. Blue contours show detection probabilities of 50%, 80%, and 95%. The hatched region below  $4 M_{\text{Jup}}$  represents where the evolutionary model is extrapolated linearly in log age space, while the sharp cutoff at  $2 M_{\text{Jup}}$  is a numerical artifact from this extrapolation (see Section 4.2 for details). The last three targets are bright and used smaller subarrays. Therefore, their maps truncate at  $\sim 30$  AU.

tifant, we extract the central column of the residual and compare with the corresponding PSF model obtained by interpolating the `stpsf` grid. Figure 10 shows that observed residual is narrower than the expected PSF profile. This suggests that this point-source-like residual is most likely an algorithmic artifact rather than real astrophysical signal.

Nevertheless, we estimate the potential mass of this residual assuming it is a substellar companion. Since the signal is located close to the image edge, forward modeling cannot be performed. Instead, we calculate the total flux on the PSF-subtracted image using an aperture with a diameter of 4.436 pixels. Flux loss due to PSF subtraction is accounted for by calculating the throughput factor at the same separation from the central star but at a diagonal position angle, under the assumption of azimuthal symmetry. We then convert the real total flux to an apparent magnitude of 16.05. This yields an apparent magnitude of 16.05. We obtain potential masses at ages of 2, 5, and 8 Gyr using the method described in Section 4.3, resulting in mass ranges of  $2.0\text{-}3.1 M_{\text{Jup}}$ ,  $2.0\text{-}4.2 M_{\text{Jup}}$ , and  $2.0\text{-}5.2 M_{\text{Jup}}$ .

609

610

611

612

613

614

615

616

617

618

619

620

621

622

623

624

625

626

627

628

629

630

631

632

633

634

635

636

637

638

639

640

641

642

643

644

645

646

647

648

649

650

651

652

653

654

## 5. DISCUSSION

### 5.1. MIRI/TSO Mode As A Planet Imager

Our analysis demonstrates that at  $15 \mu\text{m}$ , this sensitivity allows the detection of Jupiter-mass gas giants at wide orbit. Such time-series imaging data enable us to fill the blank of exoplanet searching at large separations, the region inaccessible by transiting or radial velocity method. Additionally, another 500 hours are approved for the Rocky World directory discretionary time (DDT) program (S. Redfield et al. 2024). Analysing method presented here enables the probing of wide-orbit planets orbiting the DDT program target.

We evaluate the direct imaging sensitivity of MIRI/TSO data by comparing it with published JWST/NIRCam and MIRI results. E. Bogat et al. (2025) demonstrated the capability of JWST/NIRCam coronagraphy at  $3\text{-}5 \mu\text{m}$  to search for sub-Jupiter mass planets at wide orbits around younger M-dwarfs, with age ranging from 24-440 Myr. They reported sensitivity to Saturn-mass ( $\sim 0.3 M_{\text{Jup}}$ ) planets at Saturn-like projected separations ( $\sim 9.5$  AU). By observing young systems with a coronagraph, the NIRCam survey can directly detect much lower mass planets than those detectable by MIRI/TSO observations of old ( $>5$  Gyr) M

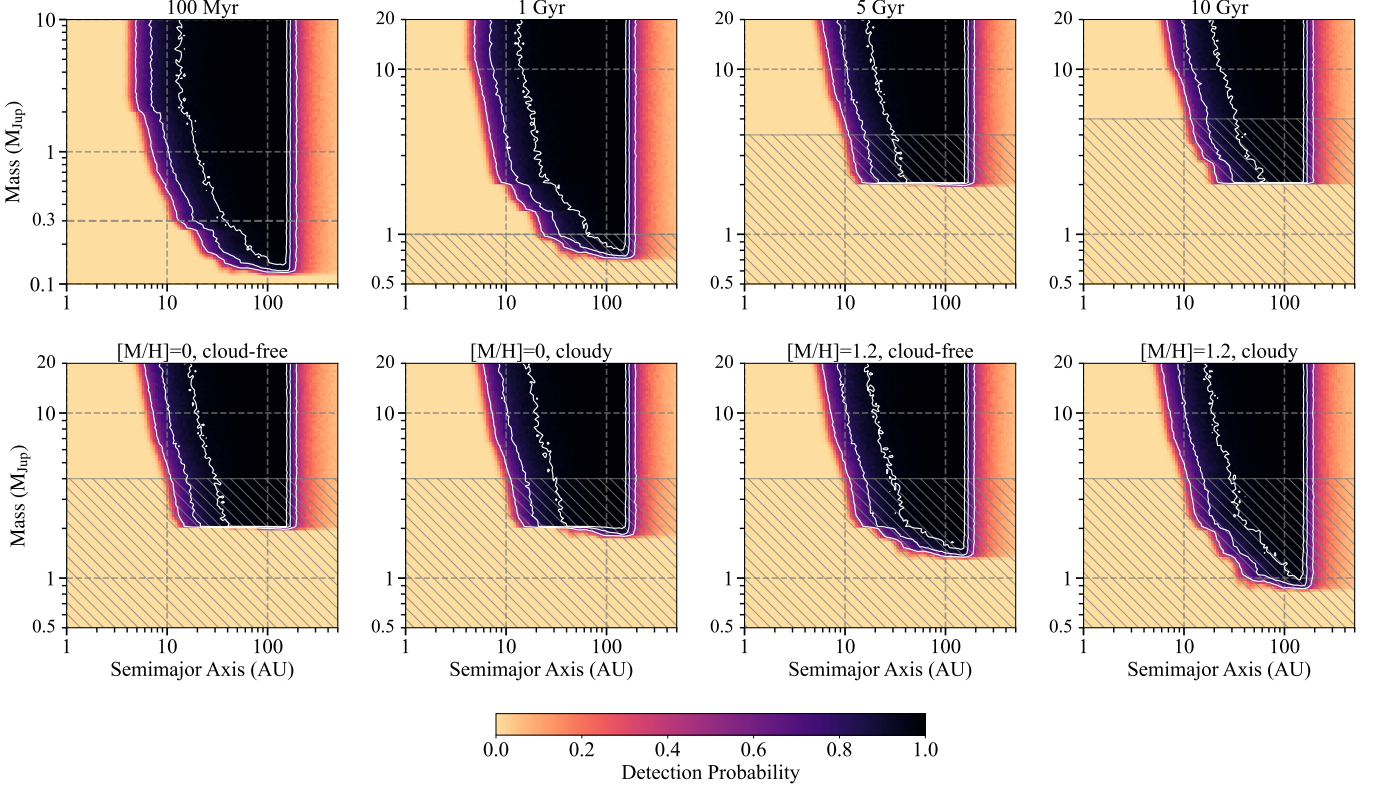


**Figure 8.** Detection probability maps for TRAPPIST-1, considering different ages or atmosphere models. *Upper panel:* Sensitivity as a function of age (100 Myr, 1 Gyr, 5 Gyr, 10 Gyr) for models with solar metallicity and cloud-free atmospheres. Detectable mass limits increase with system age. The 100 Myr map uses a different mass range to reveal the deeper sensitivity at young ages. *Lower panel:* Sensitivity as a function of atmospheric properties at fixed age (5 Gyr), showing that detectable mass limits decrease with increasing metallicity and the presence of clouds. The hatched region represents where the evolutionary model is extrapolated linearly in log age space, while the sharp cutoff at  $2 M_{Jup}$  is a numerical artifact from this extrapolation (see Section 4.2 for details).

dwarfs. The NIRCam survey targeted young M-dwarfs with ages younger than 440 Myr, while the typical age of our targets is  $\sim 5$  Gyr. According to the planet evolutionary models, planets cool and dim as they age. Therefore, beyond the age of 5 Gyr, only the most massive planets remain warm enough to produce thermal emission detectable by JWST/MIRI. Additionally, their use of coronagraphy effectively suppresses starlight. Another contributor is the fact that MIRI PSF is wider because of the larger diffraction limit. These factors combined contribute to their deeper contrast curves, with a median  $5\sigma$  sensitivity of  $1.5 \times 10^{-5}$  at  $1''$ , and a lower planet mass detection limit. While our survey does not reach the same mass sensitivity, it is suited for studying older M-dwarf planetary systems. For planets older than 5 Gyr, the peak of their thermal emission shifts to longer wavelength in the mid-infrared. Therefore, our work at  $15 \mu m$  provides a valuable window into the population of mature, evolved gas giants at wide separations.

Additionally, we compare our results to dedicated MIRI high-contrast imaging surveys. R. Bowens-Rubin

et al. (2025) reported a  $5\sigma$  contrast of  $\sim 10^{-3}$  at  $1''$  with F2100W ( $21 \mu m$ ), corresponding to an apparent magnitude of  $\sim 12.5$  mag (see their Figure 2c). The  $3\sigma$  background-limited region is reached at  $2.5''$ , corresponding to an apparent magnitude between 15.5-16 mag. They demonstrated that around Wolf 359, a solar-metallicity M6 M-dwarf with an age between 0.1-1.5 Gyr at 2.4 pc, a planet the same absolute magnitude of Saturn could be detected using MIRI imaging at  $21 \mu m$ . Our median contrast curve is  $\sim 3$  magnitude deeper than theirs, which can be partly explained by the wider PSF at longer wavelengths. Nevertheless, since the thermal emission of cold planets peaks at longer wavelengths, their survey achieves lower detectable planet mass limit. In another survey, S. Poulsen et al. (2024) obtained a  $5\sigma$  contrast of  $1.1 \times 10^{-2}$  at  $0.654''$  and a median contrast of  $6 \times 10^{-3}$  beyond  $1.26''$ , around a white dwarf at 22.4 pc with F1500W at  $15 \mu m$ <sup>10</sup>. Overall, these comparisons

<sup>10</sup> They converted their sensitivity to a planet of  $0.5 M_{Jup}$  at 3 Gyr using HELIOS models. While this planet mass limit is lower

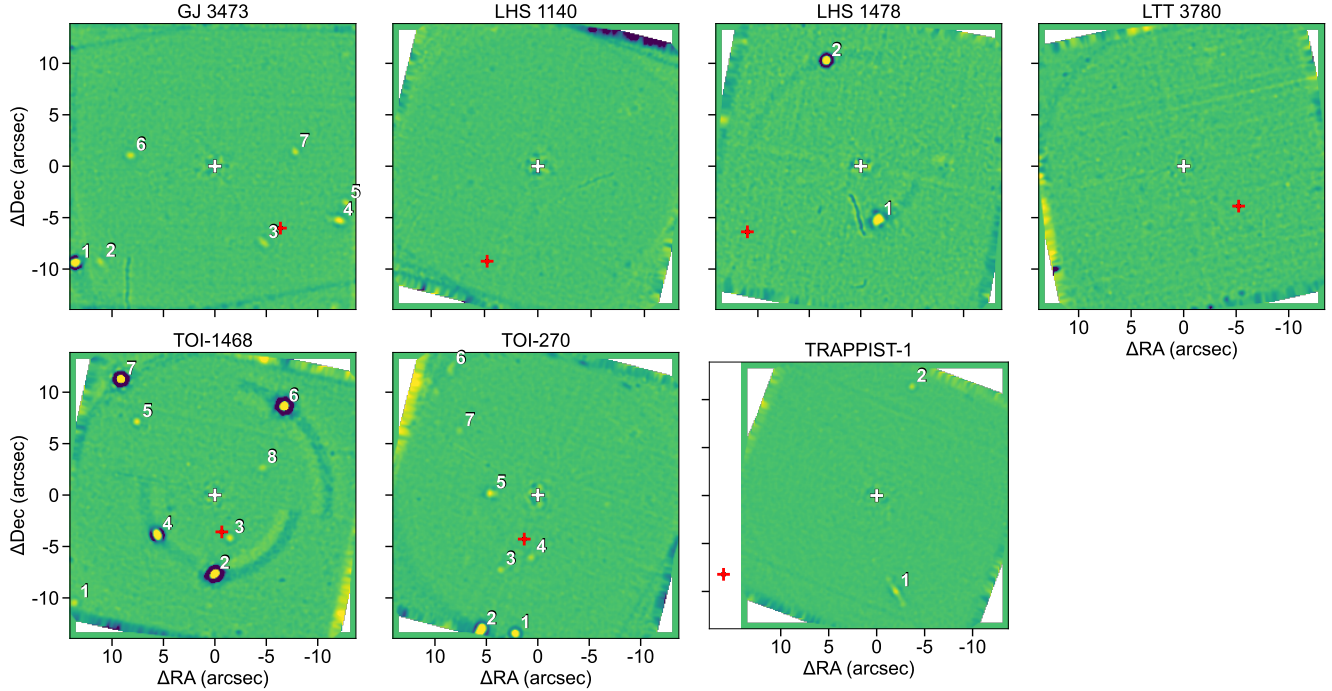


**Figure 9.** PSF subtracted images of all targets, convolved with a Gaussian kernel to better reveal close companion sources. The central star position is denoted by the white cross. Detected sources are labeled, and their astrometry and photometry properties are achieved in Table 3. The red cross on each subplot represents the position of the target star at J2040. The plots show that the target star and the companion sources (assuming background objects) could get close due to differences between their proper motions. Future observations might need to take this issue into account.

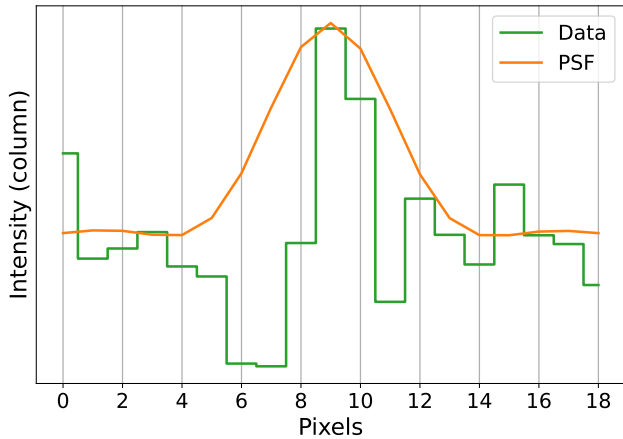


**Figure 10.** Comparison of observed point-source-like residual to PSF model prediction for HD 260655. The green line represents data extracted from the PSF-subtracted image, and the orange line shows the PSF model from interpolating the `stpsf` grid.

than ours, it partly comes from the discrepancy between the `petitCODE` and the `HELIOS` atmosphere models.

694 demonstrate that MIRI/TSO data are comparable to  
695 dedicated MIRI imaging observations in terms of high-  
696 contrast imaging performance.

697 Furthermore, we checked published Adaptive Optics  
698 results for our targets. GJ 3473 (J. Kemmer et al.  
699 2020), LTT 3780 (R. Cloutier et al. 2020), TOI-1468  
700 (P. Chaturvedi et al. 2022), HD 260655 (R. Luque et al.  
701 2022), and L 98-59 (V. B. Kostov et al. 2019) have pre-  
702 vious AO observations in the Br  $\gamma$  band, with a median  
703 contrast of  $\sim 6.5$  mag at  $0.5''$ . These results indicate no  
704 detectable companions within the field of view for these  
705 targets.

## 706 5.2. Contrast-Exposure Time Relationship

707 We investigate the relationship between contrast and  
708 exposure time using 50 images (total exposure time:  
709 18.89 hours) of TRAPPIST-1 from GTO-1177. We  
710 optimize the PSF model for the entire sequence and keep  
711 it identical for all frames (obtained as described in Sec-  
712 tion 3.4) and subtract it from individual frames. We  
713 then co-add subsets of the sequence and calculate 5-  
714 sigma contrast at separations of  $0.5''$ ,  $1''$ , and  $5''$  for  
715 subsets with various total exposure times. The con-  
716 trast versus exposure time trend depends strongly on  
717 image order. To mitigate this variation, we randomize

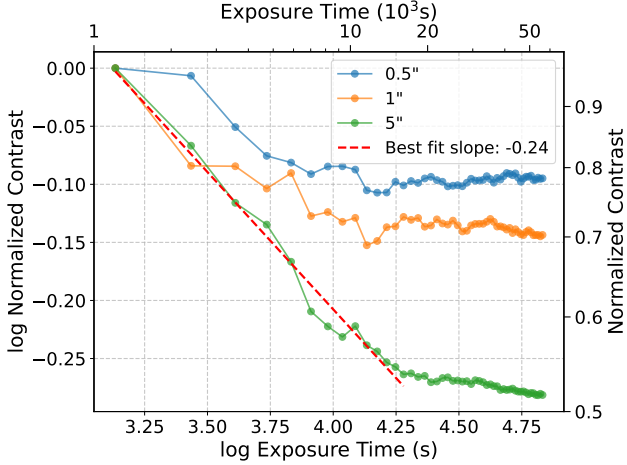


**Figure 11.** Contrast versus exposure time for TRAPPIST-1 at three angular separations. Blue, orange, and green points represent the median contrast at 0.5'', 1'', and 5'' separations, respectively, computed from ten randomized stacking trials. The red dashed line indicates a linear fit to the initial regime at 5'', with a slope of -0.24. Contrast improvement plateaus beyond  $\sim 8,000$ s for 0.5'' and beyond  $\sim 20,000$  s for 5'' separation.

the order and repeat the procedure ten times. We then calculate the median contrast-exposure time relation.

Figure 11 shows the resulting relationship in log-log space. To compare the curve shapes, the three curves are normalized by their initial contrast values. Raw contrast improves with increasing exposure time before reaching a plateau. The transition occurs at approximately 8,000 s for 0.5'' and 20,000 s for 5''. This trend aligns with expectations: at smaller separations, contrast is dominated by PSF subtraction residuals rather than photon noise, so longer exposures provide diminishing returns once systematic errors dominate. The fitted slope in the initial regime at 5'' is -0.24. This is shallower than the photon noise-limited expectation of -0.5. The deviation likely reflects systematic noise sources that average down more slowly than photon noise.

### 5.3. Gas Giants In Multi-Planet Systems

Our search and its expansion complement previous studies of the relationship between wide-orbit gas giants and close-in terrestrial planets ( $P(GG | E)$ ). M. L.

Bryan & E. J. Lee (2024) reported a distinct positive correlation between inner super-Earths and outer gas giants for solar-mass, metal-rich host stars. While the gas giant frequency is higher around metal-rich M-dwarfs, no significant correlations between super-Earths and gas giants has been established (M. L. Bryan & E. J. Lee 2025). In our study, we did not detect any wide-orbit companions around our target stars within 50 AU, despite the fact that all of them host transiting terrestrial planets. Due to the limitation of traditional trasiting and RV method, previous work has focused on separations between 0.1-10 AU. Our results provide new data points at larger separations ( $> 10$  AU), which may assist future study on M-dwarf planetary system.

Our work enables the exploration of the connection between inner planetary system architecture and the occurrence of outer gas giants around M-dwarfs. M. Y. He & L. M. Weiss (2023) presented that inner planetary systems around solar-type stars tend to have higher gap complexities ( $C$ ), a measure of the deviation from uniform spacings, when they also have outer gas giants than when they do not. We examine if similar gap complexity and planet occurence relation exists in M-dwarfs. Using the orbital period data from the NASA Exoplanet Archive, we comput the gap complexity for four systems of our targets with three or more known planets: TOI-270 (0.064), TRAPPIST-1 (0.019), L 98-59 (0.021), and GJ 357 (0.372). For comparison, M. Y. He & L. M. Weiss (2023) found a median value of  $C \sim 0.06$  for systems without outer giants, and  $C > 0.32$  for those with outer giant(s). While GJ 357 inner system has relatively high gap complexity comparable to systems with outer giants, we did not detect any companions within 20 AU down to a mass limit of  $2 M_{Jup}$ . A statistically robust evaluation of this trend rely on improved age constraints, planetary evolutionary models, and a larger target sample. While our results cannot put new statistical constrains on the theory, we provide a way to study the architecture of M-dwarf systems. The reduction and analysis approach presented in this paper can be applied to more similar time-series data. With large enough datasets, we could put new constrains on the relation between inner and outer planets around M-dwarfs and futher understand the gap complexity of its planetary systems.

**Table 3.** Background Sources Astrometry And Photometry Properties

Source	$\Delta\text{RA}$ (arcsec)	$\Delta\text{Dec}$ (arcsec)	Separation (AU)	Mag	S/N	FWHM Major (pixels)	FWHM Minor (pixels)	Mass(1 Gyr) ( $M_{\text{Jup}}$ )	Mass(5 Gyr) ( $M_{\text{Jup}}$ )	Mass(10 Gyr) ( $M_{\text{Jup}}$ )
GJ 3473-1	13.49 $\pm$ 0.00	-9.36 $\pm$ 0.00	448.63	13.03 $\pm$ 0.02	57.4	5.1 $\pm$ 0.1*	4.3 $\pm$ 0.1*	36.4	71.9	74.7
GJ 3473-2	11.06 $\pm$ 0.04	-9.26 $\pm$ 0.05	394.08	16.79 $\pm$ 0.17	6.1	6.8 $\pm$ 0.7	3.1 $\pm$ 0.3	—	—	—
GJ 3473-3	-4.75 $\pm$ 0.04	-7.43 $\pm$ 0.04	241.04	17.12 $\pm$ 0.13	8.0	8.0 $\pm$ 0.6	3.3 $\pm$ 0.3	Extended	—	—
GJ 3473-4	-12.00 $\pm$ 0.02	-5.25 $\pm$ 0.02	357.99	15.08 $\pm$ 0.07	15.7	6.9 $\pm$ 0.3	3.7 $\pm$ 0.2	Extended	—	—
GJ 3473-5	-12.68 $\pm$ 0.04	-3.54 $\pm$ 0.03	359.78	15.81 $\pm$ 0.14	7.7	5.2 $\pm$ 0.5	2.8 $\pm$ 0.3	3.2	9.2	14.2
GJ 3473-6	8.15 $\pm$ 0.03	1.06 $\pm$ 0.02	224.63	16.81 $\pm$ 0.09	11.9	5.0 $\pm$ 0.4	3.7 $\pm$ 0.3	2.0-2.1	4.3	6.7
GJ 3473-7	-7.76 $\pm$ 0.03	1.42 $\pm$ 0.03	215.64	17.04 $\pm$ 0.12	8.4	4.8 $\pm$ 0.4	3.2 $\pm$ 0.3	2.0	2.0-4.2	5.7
LHS 1478-1	-1.75 $\pm$ 0.01	-5.16 $\pm$ 0.01	99.32	15.05 $\pm$ 0.04	24.1	6.0 $\pm$ 0.2	4.7 $\pm$ 0.1	Extended	—	—
LHS 1478-2	3.30 $\pm$ 0.00	10.25 $\pm$ 0.00	196.16	14.04 $\pm$ 0.02	53.6	3.6 $\pm$ 0.1	3.3 $\pm$ 0.1	6.8	19.3	29.3
TOI-270-1	2.16 $\pm$ 0.01	-13.43 $\pm$ 0.01	305.83	13.80 $\pm$ 0.04	24.7	4.6 $\pm$ 0.1*	4.1 $\pm$ 0.1*	12.0	36.4	49.9
TOI-270-3	3.55 $\pm$ 0.03	-7.24 $\pm$ 0.02	181.26	17.20 $\pm$ 0.10	10.3	4.0 $\pm$ 0.4	3.4 $\pm$ 0.3	1.7	2.0-4.2	2.0-5.3
TOI-270-4	0.60 $\pm$ 0.03	-6.05 $\pm$ 0.03	136.74	17.33 $\pm$ 0.11	9.6	4.8 $\pm$ 0.4	3.7 $\pm$ 0.3	1.6	2.0-4.2	2.0-5.3
TOI-270-5	4.59 $\pm$ 0.02	0.19 $\pm$ 0.02	103.24	16.44 $\pm$ 0.07	14.1	4.3 $\pm$ 0.2	3.9 $\pm$ 0.2	2.0-2.1	2.0-4.2	6.4
TOI-270-6	8.50 $\pm$ 0.07	12.24 $\pm$ 0.09	335.07	17.59 $\pm$ 0.35	3.0	8.8 $\pm$ 1.0	3.5 $\pm$ 0.4	Extended	—	—
TOI-270-7	7.56 $\pm$ 0.05	6.25 $\pm$ 0.05	220.48	17.92 $\pm$ 0.22	4.7	4.3 $\pm$ 0.6	3.7 $\pm$ 0.5	1.3	2.0-4.2	2.0-5.3
TOI-1468-1	13.60 $\pm$ 0.06	-10.42 $\pm$ 0.07	423.49	16.47 $\pm$ 0.38	2.8	5.3 $\pm$ 0.6*	5.0 $\pm$ 0.6*	2.0-2.1	4.8	7.4
TOI-1468-2	-0.00 $\pm$ 0.00	-7.62 $\pm$ 0.00	188.41	13.03 $\pm$ 0.01	162.2	4.5 $\pm$ 0.1	3.4 $\pm$ 0.1	31.1	68.9	73.5
TOI-1468-3	-1.45 $\pm$ 0.02	-4.14 $\pm$ 0.02	108.49	16.73 $\pm$ 0.09	11.2	4.1 $\pm$ 0.3	3.7 $\pm$ 0.3	2.0-2.1	2.0-4.2	6.0
TOI-1468-4	5.59 $\pm$ 0.00	-3.83 $\pm$ 0.01	167.52	14.29 $\pm$ 0.02	47.6	5.0 $\pm$ 0.1	3.4 $\pm$ 0.1	Extended	—	—
TOI-1468-5	7.56 $\pm$ 0.06	7.15 $\pm$ 0.05	257.31	16.44 $\pm$ 0.30	3.5	3.5 $\pm$ 0.2	3.4 $\pm$ 0.2	2.0-2.1	4.9	7.7
TOI-1468-6	-6.71 $\pm$ 0.00	8.63 $\pm$ 0.00	270.36	12.92 $\pm$ 0.01	178.1	4.0 $\pm$ 0.1	3.7 $\pm$ 0.1	33.7	70.5	74.1
TOI-1468-7	9.08 $\pm$ 0.00	11.25 $\pm$ 0.00	357.48	12.84 $\pm$ 0.01	156.8	3.5 $\pm$ 0.1	3.3 $\pm$ 0.1	35.9	71.6	74.6
TOI-1468-8	-4.61 $\pm$ 0.04	2.67 $\pm$ 0.03	131.76	17.35 $\pm$ 0.16	6.7	5.6 $\pm$ 0.6	3.7 $\pm$ 0.4	1.7	2.0-4.2	2.0-5.3
TRAPPIST-1-1	-1.99 $\pm$ 0.01	-9.96 $\pm$ 0.01	126.60	15.66 $\pm$ 0.05	21.4	10.0 $\pm$ 0.5	3.1 $\pm$ 0.2	Background source	—	—
TRAPPIST-1-2	-3.66 $\pm$ 0.01	11.36 $\pm$ 0.01	148.83	16.09 $\pm$ 0.06	16.8	3.6 $\pm$ 0.3	3.1 $\pm$ 0.3	Background source	—	—

**Table 3** *continued*

Table 3 (*continued*)

## 6. SUMMARY

Our findings are:

- We re-analyzed JWST/MIRI F1500W ( $15\mu\text{m}$ ) TSO data of ten intensively studied transiting planet systems and perform direct imaging search for wide-orbit gas giant planets. The ten targets are cross-referenced as PSF reference stars, which supports a successful implementation of reference star differential imaging data reduction. We follow J. I. Adams Redai et al. (2023) and establish a robust framework to optimize PSF subtraction using the KLIP algorithms (Figure 2). Our analysis deliver the deepest  $15\mu\text{m}$  images of our targets (Figures 4 and 5)
  - We achieved a median  $5\sigma$  sensitivity of  $1.5 \times 10^{-3}$  (median apparent magnitude of 16.4 mag) at a separation of  $1''$  and  $2.1 \times 10^{-4}$  (18.5 mag) at separations  $\gtrsim 3''$  (Figure 6). Assuming 5 Gyr system age, cloud-free, and solar metallicity atmosphere model, we can detect  $> 2 M_{\text{Jup}}$  planet with a 95% probability beyond 50 AU in seven targets (Figure 7). The detectable mass limit increases with the assumed system age and the sensitivity estimates strongly rely on extrapolating the available planet evolutionary models when system age exceeds 5 Gyr.
  - Within 50 AU projected separation, we found a point-like close companion to HD 260655 with a peak S/N of 4.86. If this feature is a substellar companion, its estimated mass ranges from  $2.0\text{--}5.2 M_{\text{Jup}}$  depending on system age. The companion source is located at the edge of the observation subarray and its shape cannot be accurately determined. To place meaningful occurrence-rate constraints on this population will require a follow-up epoch of observations to confirm or refute the candidates found by this study.
  - Beyond 50 AU projected separation, we detected 25 uncataloged sources with high confidence ( $S/N > 5$ ). Table 3 summarizes their relative positons to

the central star, detection S/N, brightness in the F1500W band, and their masses based on cooling tracks (assuming that they are substellar companions). If all 25 sources are background stars or galaxies, four of them will be within five arcsec separation to the planet hosts within five years and impact future transit observations.

5. Our work enhances the value of MIRI TSO imaging data. The sensitivity in direct detecting planets is competitive against dedicated MIRI imaging surveys. Although the detectable mass limit is higher than NIRCam coronagraphic imaging targeting younger stars, the superior sensitivity to old gas giant planets creates a new way to probe the wide-orbit gas giant planet population. We advocate including the high-contrast imaging analysis as part of the standard routine in processing MIRI TSO imaging observations of transit planet systems.

## ACKNOWLEDGEMENTS

Y.L. and Y.Z. acknowledge support from Heising-Simons Foundation 51 Pegasi b Alumni Faculty Grant (2023-4808 – 51). We acknowledge support from the Virginia Initiative for Cosmic Origins (VICO) summer program, during which portions of this work were completed. This work is based on observations made with the NASA/ESA/CSA James Webb Space Telescope. The data were obtained from the Mikulski Archive for Space Telescopes at the Space Telescope Science Institute, which is operated by the Association of Universities for Research in Astronomy, Inc., under NASA contract NAS 5-03127 for JWST. These observations are associated with program GTO-1177, GO-2304, GO-3077, and GO-3730.

Facilities: JWST

*Software:* jwst, pyklip, photutils, astropy, umpy, scipy, matplotlib

## REFERENCES

- 860 Adams Redai, J. I., Follette, K. B., Wang, J., et al. 2023,  
861 AJ, 165, 57, doi: [10.3847/1538-3881/aca60d](https://doi.org/10.3847/1538-3881/aca60d)  
862 Allen, N. H., Espinoza, N., Diamond-Lowe, H., et al. 2025,  
863 AJ, 170, 240, doi: [10.3847/1538-3881/adfc51](https://doi.org/10.3847/1538-3881/adfc51)  
864 August, P. C., Buchhave, L. A., Diamond-Lowe, H., et al.  
865 2025, A&A, 695, A171,  
866 doi: [10.1051/0004-6361/202452611](https://doi.org/10.1051/0004-6361/202452611)  
867 Balmer, W. O., Bardalez Gagliuffi, D., Pueyo, L., et al.  
868 2025, arXiv e-prints, arXiv:2506.09201

- 869 Boccaletti, A., Lagage, P.-O., & Baudoz, P. 2024,  
 870 *Astronomy & Astrophysics*, 686, A33,  
 871 doi: [10.1051/0004-6361/202348771](https://doi.org/10.1051/0004-6361/202348771)
- 872 Bogat, E., Schlieder, J. E., Lawson, K. D., et al. 2025,  
 873 <https://arxiv.org/abs/2504.11659>
- 874 Bowens-Rubin, R., Mang, J., & Limbach, M. A. 2025, *The  
 875 Astrophysical Journal*, 986, L26,  
 876 doi: [10.3847/2041-8213/ada6b9](https://doi.org/10.3847/2041-8213/ada6b9)
- 877 Bradley, L., Sipőcz, B., Robitaille, T., et al. 2025,, 2.1.0  
 878 Zenodo, doi: [10.5281/zenodo.14606896](https://doi.org/10.5281/zenodo.14606896)
- 879 Bryan, M. L., & Lee, E. J. 2024, *ApJL*, 968, L25,  
 880 doi: [10.3847/2041-8213/ad4993](https://doi.org/10.3847/2041-8213/ad4993)
- 881 Bryan, M. L., & Lee, E. J. 2025, *ApJL*, 982, L7,  
 882 doi: [10.3847/2041-8213/adb0bd](https://doi.org/10.3847/2041-8213/adb0bd)
- 883 Burdanov, A. Y., de Wit, J., Brož, M., et al. 2024, *Nature*,  
 884 638, 74, doi: [10.1038/s41586-024-08480-z](https://doi.org/10.1038/s41586-024-08480-z)
- 885 Burgasser, A. J., & Mamajek, E. E. 2017, *ApJ*, 845, 110,  
 886 doi: [10.3847/1538-4357/aa7fea](https://doi.org/10.3847/1538-4357/aa7fea)
- 887 Carmona, A., Delfosse, X., Bellotti, S., et al. 2023, *A&A*,  
 888 674, A110, doi: [10.1051/0004-6361/202346063](https://doi.org/10.1051/0004-6361/202346063)
- 889 Chaturvedi, P., Bluhm, P., Nagel, E., et al. 2022, *A&A*,  
 890 666, A155, doi: [10.1051/0004-6361/202244056](https://doi.org/10.1051/0004-6361/202244056)
- 891 Cloutier, R., Eastman, J. D., Rodriguez, J. E., et al. 2020,  
 892 *AJ*, 160, 3, doi: [10.3847/1538-3881/ab91c2](https://doi.org/10.3847/1538-3881/ab91c2)
- 893 Dittmann, J. A., Irwin, J. M., Charbonneau, D., et al.  
 894 2017, *Nature*, 544, 333, doi: [10.1038/nature22055](https://doi.org/10.1038/nature22055)
- 895 Ducrot, E., Lagage, P.-O., Min, M., et al. 2025, *Nature  
 896 Astronomy*, 9, 358, doi: [10.1038/s41550-024-02428-z](https://doi.org/10.1038/s41550-024-02428-z)
- 897 Engle, S. G., & Guinan, E. F. 2023, *ApJL*, 954, L50,  
 898 doi: [10.3847/2041-8213/acf472](https://doi.org/10.3847/2041-8213/acf472)
- 899 Fortune, M., Gibson, N. P., Diamond-Lowe, H., et al. 2025,  
 900 *A&A*, 701, A25, doi: [10.1051/0004-6361/202554198](https://doi.org/10.1051/0004-6361/202554198)
- 901 Franson, K., Bowler, B. P., & Zhou, Y. 2024, *The  
 902 Astrophysical Journal*, 974, L11,  
 903 doi: [10.3847/2041-8213/ad73da](https://doi.org/10.3847/2041-8213/ad73da)
- 904 Gaia Collaboration, Prusti, T., de Bruijne, J. H. J., et al.  
 905 2016, *A&A*, 595, A1, doi: [10.1051/0004-6361/201629272](https://doi.org/10.1051/0004-6361/201629272)
- 906 Gaia Collaboration, Vallenari, A., Brown, A. G. A., et al.  
 907 2023, *A&A*, 674, A1, doi: [10.1051/0004-6361/202243940](https://doi.org/10.1051/0004-6361/202243940)
- 908 Gillon, M., Triaud, A. H. M. J., Demory, B.-O., et al. 2017,  
 909 *Nature*, 542, 456, doi: [10.1038/nature21360](https://doi.org/10.1038/nature21360)
- 910 Gillon, M., Ducrot, E., Bell, T. J., et al. 2025, arXiv  
 911 e-prints, arXiv:2509.02128,  
 912 doi: [10.48550/arXiv.2509.02128](https://doi.org/10.48550/arXiv.2509.02128)
- 913 Greene, T. P., Bell, T. J., Ducrot, E., et al. 2023, *Nature*,  
 914 618, 39, doi: [10.1038/s41586-023-05951-7](https://doi.org/10.1038/s41586-023-05951-7)
- 915 Gupta, P., Atreya, S. K., Steffes, P. G., et al. 2022, in EGU  
 916 General Assembly Conference Abstracts, EGU General  
 917 Assembly Conference Abstracts, EGU22-966,  
 918 doi: [10.5194/egusphere-egu22-966](https://doi.org/10.5194/egusphere-egu22-966)
- 919 He, M. Y., & Weiss, L. M. 2023, *AJ*, 166, 36,  
 920 doi: [10.3847/1538-3881/acdd56](https://doi.org/10.3847/1538-3881/acdd56)
- 921 Kammerer, J., Lawson, K., Perrin, M. D., et al. 2024, *AJ*,  
 922 168, 51, doi: [10.3847/1538-3881/ad4ffe](https://doi.org/10.3847/1538-3881/ad4ffe)
- 923 Kemmer, J., Stock, S., Kossakowski, D., et al. 2020, *A&A*,  
 924 642, A236, doi: [10.1051/0004-6361/202038967](https://doi.org/10.1051/0004-6361/202038967)
- 925 Kostov, V. B., Schlieder, J. E., Barclay, T., et al. 2019, *AJ*,  
 926 158, 32, doi: [10.3847/1538-3881/ab2459](https://doi.org/10.3847/1538-3881/ab2459)
- 927 Lagrange, A.-M., et al. 2025, *Nature*,  
 928 doi: [10.1038/s41586-025-09150-4](https://doi.org/10.1038/s41586-025-09150-4)
- 929 Limbach, M. A., Vanderburg, A., & Stevenson, K. B. 2024,  
 930 *The Astrophysical Journal*, 973, L11,  
 931 doi: [10.3847/2041-8213/ad6866](https://doi.org/10.3847/2041-8213/ad6866)
- 932 Linder, E. F., Mordasini, C., Mollière, P., et al. 2019, *A&A*,  
 933 623, A85, doi: [10.1051/0004-6361/201833873](https://doi.org/10.1051/0004-6361/201833873)
- 934 Luque, R., Fulton, B. J., Kunimoto, M., et al. 2022, *A&A*,  
 935 664, A199, doi: [10.1051/0004-6361/202243834](https://doi.org/10.1051/0004-6361/202243834)
- 936 Matthews, E. C., Carter, A. L., Pathak, P., et al. 2024,  
 937 *Nature*, 633, 789, doi: [10.1038/s41586-024-07837-8](https://doi.org/10.1038/s41586-024-07837-8)
- 938 Meier Valdés, E. A., Demory, B.-O., Diamond-Lowe, H.,  
 939 et al. 2025, *A&A*, 698, A68,  
 940 doi: [10.1051/0004-6361/202453449](https://doi.org/10.1051/0004-6361/202453449)
- 941 Penny, M. T., Scott Gaudi, B., Kerins, E., et al. 2019, *The  
 942 Astrophysical Journal Supplement Series*, 241, 3,  
 943 doi: [10.3847/1538-4365/aafb69](https://doi.org/10.3847/1538-4365/aafb69)
- 944 Phillips, M. W., Tremblin, P., Baraffe, I., et al. 2020, *A&A*,  
 945 637, A38, doi: [10.1051/0004-6361/201937381](https://doi.org/10.1051/0004-6361/201937381)
- 946 Poulsen, S., Debes, J., Cracraft, M., et al. 2024, *AJ*, 167,  
 947 257, doi: [10.3847/1538-3881/ad374c](https://doi.org/10.3847/1538-3881/ad374c)
- 948 Powell, D., Feinstein, A. D., Lee, E. K. H., et al. 2024,  
 949 *Nature*, 626, 979, doi: [10.1038/s41586-024-07040-9](https://doi.org/10.1038/s41586-024-07040-9)
- 950 Pueyo, L. 2016, *ApJ*, 824, 117,  
 951 doi: [10.3847/0004-637X/824/2/117](https://doi.org/10.3847/0004-637X/824/2/117)
- 952 Redfield, S., Batalha, N., Benneke, B., et al. 2024,  
 953 doi: [10.48550/arXiv.2404.02932](https://doi.org/10.48550/arXiv.2404.02932)
- 954 Soummer, R., Pueyo, L., & Larkin, J. 2012, *ApJL*, 755,  
 955 L28, doi: [10.1088/2041-8205/755/2/L28](https://doi.org/10.1088/2041-8205/755/2/L28)
- 956 Stolk, T., Quanz, S. P., Todorov, K. O., et al. 2020, *A&A*,  
 957 635, A182, doi: [10.1051/0004-6361/201937159](https://doi.org/10.1051/0004-6361/201937159)
- 958 Valentine, D., Wakeford, H. R., Challener, R. C., et al.  
 959 2024, *AJ*, 168, 123, doi: [10.3847/1538-3881/ad5c61](https://doi.org/10.3847/1538-3881/ad5c61)
- 960 Zieba, S., Kreidberg, L., Ducrot, E., et al. 2023, *Nature*,  
 961 620, 746, doi: [10.1038/s41586-023-06232-z](https://doi.org/10.1038/s41586-023-06232-z)